Journal of Computational Physics 228 (2009) 7025–7045

Contents lists available at ScienceDirect

Journal of Computational Physics

journal homepage: www.elsevier.com/locate/jcp

Effect of randomness on multi-frequency aeroelastic responses resolved by Unsteady Adaptive Stochastic Finite Elements

Jeroen A.S. Witteveen *, Hester Bijl

Faculty of Aerospace Engineering, Delft University of Technology, Kluyverweg 1, 2629HS Delft, The Netherlands

ARTICLE INFO

Article history:
Received 11 August 2008
Received in revised form 16 April 2009
Accepted 15 June 2009
Available online 23 June 2009

Keywords:
Stochastic Finite Elements
Fluid–structure interaction
Multi-frequency response
Wavelets

ABSTRACT

The Unsteady Adaptive Stochastic Finite Elements (UASFE) method resolves the effect of randomness in numerical simulations of single-mode aeroelastic responses with a constant accuracy in time for a constant number of samples. In this paper, the UASFE framework is extended to multi-frequency responses and continuous structures by employing a wavelet decomposition pre-processing step to decompose the sampled multi-frequency signals into single-frequency components. The effect of the randomness on the multi-frequency response is then obtained by summing the results of the UASFE interpolation at constant phase for the different frequency components. Results for multi-frequency responses and continuous structures show a three orders of magnitude reduction of computational costs compared to crude Monte Carlo simulations in a harmonically forced oscillator, a flutter panel problem, and the three-dimensional transonic AGARD 445.6 wing aeroelastic benchmark subject to random fields and random parameters with various probability distributions.

1. Introduction

Numerical errors in industrial simulations nowadays start to reach acceptable engineering accuracy levels. As a consequence, physical variability tends to dominate the error in numerical predictions. Inherent physical variations are present in virtually all engineering applications due to, for example, varying atmospheric conditions and production tolerances. Accounting for physical variations is, therefore, vital for making reliable predictions, which can be utilized in robust design optimization and reducing design safety factors. To this end, we are interested in determining the full probability distribution and the central moments of the output of interest. In contrast, in structural reliability analysis [6] one propagates input randomness to compute the probability of failure. Structural failure is then defined as the point where selected limit state functions exceed their limits for failure [22]. Failure probabilities are often small such that in reliability analysis one pursues the tails of the distribution instead of the statistical moments.

An intuitive uncertainty quantification method for propagating physical input variations to the output probability distribution is Monte Carlo simulation [14]. However, solving many deterministic problems for randomly varying parameter values simply leads to impractically high computational costs for problems which are already computationally intensive in the deterministic case, such as computational fluid dynamics and fluid–structure interaction simulations. More efficient non-intrusive Polynomial Chaos methods [16,27] aim at reducing the number of deterministic computations by using a global polynomial interpolation of the samples in parameter space. An effective sampling in suitable Gauss quadrature points is employed in Probabilistic Collocation (PC) approaches [2,23,28]. Other Polynomial Chaos formulations [1,13,32,39] construct a polynomial approximation of the response based on Hilbert space projections of suitable orthogonal polynomial bases. A

* Corresponding author. Tel.: +31 15 27 85773; fax: +31 15 27 87077.
E-mail address: j.a.s.witteveen@tudelft.nl (J.A.S. Witteveen).

0021-9991/$ - see front matter © 2009 Elsevier Inc. All rights reserved.
doi:10.1016/j.jcp.2009.06.013

more robust approximation is achieved by multi-element Adaptive Stochastic Finite Elements (ASFE) methods [11,19,20,31,37], which employ a piecewise polynomial interpolation of the samples. Due to these developments the efficient propagation of physical randomness has become possible over the last decade for steady computational problems with not too many random input parameters such as in [34]. For high-dimensional probability spaces the tensor quadrature methods suffer from the curse-of-dimensionality with an exponentially increasing sample size with the number of random parameters. In contrast for Monte Carlo methods the number of required samples to reach a target accuracy is independent of the dimension of the problem.

One of the current challenges in modeling physical variability in computationally intensive problems is unsteadiness. The trend towards unsteady simulations in computational fluid dynamics and high fidelity post-flutter predictions in fluid–structure interaction dictates also an increasing application of uncertainty quantification to time-dependent problems. However, uncertainty quantification methods usually require a fast increasing number of samples with time to resolve the large effect of random parameters in these dynamical systems with a constant accuracy. The increasing sample size is caused by the increasing nonlinearity of the response surface [26] due to the effect of the random parameters on the frequency and, consequently, on the increasing phase differences in time for oscillatory responses. Resolving the asymptotic effect of physical variations, which is of practical interest in post-flutter analysis [4], can, therefore, easily lead to thousands of required deterministic simulations. For oscillatory time-dependent responses a Fourier Chaos basis [24] has recently been proposed.

Two alternative Unsteady Adaptive Stochastic Finite Elements (UASFE) methodologies [35,36] developed by the authors achieve a constant accuracy in time with a constant number of samples, in contrast with the usually fast increasing number of samples required by other methods. The first UASFE formulation is based on uncertainty quantification interpolation of a time-independent parameterization of oscillatory samples [33,35] instead of the time-dependent samples themselves. This time-independent parameterization, developed both in combination with a global polynomial interpolation in [33] and a multi-element ASFE interpolation in [35], results in an interpolation accuracy which is independent of time. In this paper, we employ an ASFE interpolation based on Newton–Cotes quadrature in simplex elements [37], since it is a non-intrusive higher-order extrema diminishing scheme in probability space that requires a low number of deterministic computations. The second UASFE methodology based on uncertainty quantification interpolation of the oscillatory samples at constant phase [36] instead of at constant time, eliminates the effect of increasing phase differences with time. The latter approach has the advantages that it is not subject to a parameterization error and that it can resolve time-dependent functionals. The merit of this framework as compared to previous approaches is that it is proven to achieve a bounded error as function of the phase for periodic responses and under certain conditions also a bounded error in time [38]. This results in practice in an approximately constant accuracy in time for a constant number of samples also for nonperiodic responses. However, in both UASFE formulations the phase of the oscillatory samples has to be well-defined. This restriction limits the application of the methodologies to single-frequency responses.

Fluid–structure interaction problems of practical importance, however, often exhibit a multi-frequency response. The different frequencies can originate from the combination of the natural frequency of the structure and the dominant frequency of the fluid forcing. The structural system can also exhibit a multi-frequency response itself. A dominant frequency in the flow forces can, for example, be caused by the Von Kármán vortex shedding in the wake of a blunt body. A multi-frequency structural response results naturally from a continuous structure with numerous eigenmodes and eigenfrequencies.

In this paper the Unsteady Adaptive Stochastic Finite Elements framework is further extended to resolve the effect of randomness on multi-frequency aeroelastic responses by employing a wavelet decomposition. The multi-frequency samples are first converted into their single-frequency components in a standard wavelet decomposition pre-processing step. The effect of the physical variations on the different frequency components is then resolved using UASFE interpolation of the single-frequency signals at constant phase. The final effect of the randomness on the multi-frequency response is obtained by summing the contributions of the single-frequency components. The multi-frequency response of a continuous structure is first projected onto either the nodal basis of a finite elements discretization or the modal basis of the natural modes of the structure in vacuum, before the wavelet decomposition is performed.

The proposed UASFE formulation for multi-frequency responses is developed in Section 2. The effect of randomness on the multi-frequency response of a single-degree-of-freedom mass–spring system with harmonic external forcing is resolved and the error convergence is assessed in Section 3.1. In Section 3.2 the stochastic multi-frequency response of a continuous panel structure in supersonic flow is analyzed using a modal projection of the structural response. The three-dimensional transonic AGARD 445.6 wing subject to random free stream flow conditions is studied in Section 3.3. A nodal representation of the continuous structure shows based on the tip-node displacement that the randomness causes a non-zero probability of flutter. The results for input random fields and random parameters with various probability distributions are compared to those of Monte Carlo simulations. The UASFE framework presented here for fluid–structure interaction simulation is also applicable to unsteady fluid dynamics and other unsteady multi-disciplinary problems.

2. Unsteady Adaptive Stochastic Finite Elements for multi-frequency responses

The wavelet decomposition of multi-frequency time series is briefly reviewed in Section 2.1. In Section 2.2 the procedure for multi-frequency responses of continuous structures is detailed. The UASFE interpolation of the single-frequency components is developed in Section 2.3. The resulting UASFE algorithm for multi-frequency responses is summarized in Section 2.4.

2.1. Wavelet decomposition of multi-frequency signals

Assume that dynamical system

$$\mathcal{L}(\mathbf{x},t,\omega;u(\mathbf{x},t,\omega)) = S(\mathbf{x},t,\omega), \tag{1}$$

with appropriate initial and boundary conditions results in an oscillatory response $u(\mathbf{x},t,\omega)$, which consists of multiple frequency components. Operator $\mathcal{L}$ and source term S are defined on domain $D \times T \times \Omega$, where $\mathbf{x} \in D$ and $t \in T$ are the spatial and temporal dimensions with $D \subset \mathbb{R}^d,\ d = \{1,2,3\}$, and $T = [0, t_{\max}]$. The argument ω denotes a realization of the set of outcomes Ω of the probability space $(\Omega, \mathcal{F}, P)$ with $\mathcal{F} \subset 2^{\Omega}$ the σ-algebra of events and P a probability measure. The probability space originates from n uncorrelated second-order random parameters $\mathbf{a}(\omega) = \{a_1(\omega), \ldots, a_n(\omega)\} \in A$ in Eq. (1) and its initial and boundary conditions.

A number of methods for decomposing multi-frequency signals in single-frequency components is readily available [8]. For example, the Fourier transform can be used to determine the frequency resolution of a signal by representing it in terms of sinusiodal functions. The Fourier transform contains, however, no localized time information. In contrast the short-time Fourier transform and the wavelet transform result in time-varying frequency information. The wavelet transform usually results in a superior multiresolution decomposition of the signal at reduced computational costs in comparison with short-time Fourier transform, which has limited frequency resolution in time.

The stochastic behavior of multi-frequency response $u(\mathbf{x},t,\omega)$ is resolved using UASFE by computing N_s deterministic samples $u_i(\mathbf{x},t)$ for varying parameter values $\mathbf{a}_i$, with $i = 1, \ldots, N_s$. The multi-frequency samples $u_i(\mathbf{x},t)$ are first decomposed into their different modes using wavelets [10,30]. The discrete wavelet transform of a signal $f(t)$ is given by

$$f(t) = \sum_a \sum_b \gamma_{a,b}\psi_{a,b}(t), \tag{2}$$

with wavelet transform coefficients $\gamma_{a,b}$ and wavelet

$$\psi_{a,b}(t) = \frac{1}{\sqrt{a}}\Psi\left(\frac{t-b}{a}\right), \tag{3}$$

scaled and translated versions of the mother wavelet $\Psi(t)$, with positive scale parameter a and real shift parameter b. The discrete wavelet transform is used here to divide the multi-frequency samples $u_i(t)$ into N_f single-frequency components $\tilde{u}_{i,k}(t)$

$$u_i(t) = \sum_{k=1}^{N_f} \tilde{u}_{i,k}(t), \tag{4}$$

see Fig. 1. The argument $\mathbf{x}$ has been dropped here for convenience in the notation. The parameters a and b are determined in a standard wavelet decomposition in an available wavelet toolbox. The required number of frequency levels N_f can be established by analyzing the deterministic system response. UASFE interpolation of the single-frequency signals $\tilde{u}_{i,k}(t)$ is then performed to resolve the effect of the randomness on the different frequency components given by the functions $\tilde{u}_k(t,\omega)$. In order to obtain an approximation of the stochastic behavior of the multi-frequency response $u(t,\omega)$ the contributions of the different frequency components are summed

$$u(t,\omega) = \sum_{k=1}^{N_f} \tilde{u}_k(t,\omega), \tag{5}$$

from which the probability distribution and statistical moments of the output, e.g. mean $\mu_u(t)$ and standard deviation $\sigma_u(t)$, can be determined using sorting and numerical integration. In order to effectively decompose a multi-mode signal using wavelet transformation, the different frequencies need to be sufficiently distinct. More precisely the single frequencies have to fall in different levels of the wavelet decomposition. A frequency separation of an order of magnitude is in this case enough. If some frequencies cannot be separated well by the wavelet decomposition, the phase of the remaining signal may not be well-defined by the algorithm for extracting the phase based on local extrema of the sample. In that case, Adaptive Stochastic Finite Elements interpolation can directly be applied to interpolate the samples at constant time. The wavelet decomposition is performed using the *Matlab* Wavelet Toolbox. In the applications Coifman's wavelets [9] are employed, which give the best results for the considered examples.

2.2. Treatment of continuous structures

Continuous structures in vacuum exhibit in general a multi-frequency response in terms of their natural modes and natural frequencies. The coupling of the structure with a flow field in a fluid–structure interaction alters the eigenmodes of the complete system. Usually the natural modes and frequencies of the coupled system are unknown due to the nonlinearity of the equations describing the flow. Therefore, both a nodal and a modal description of the structural response in terms of, respectively, the degrees-of-freedom of a finite element discretization or the natural modes of the structure in vacuum result

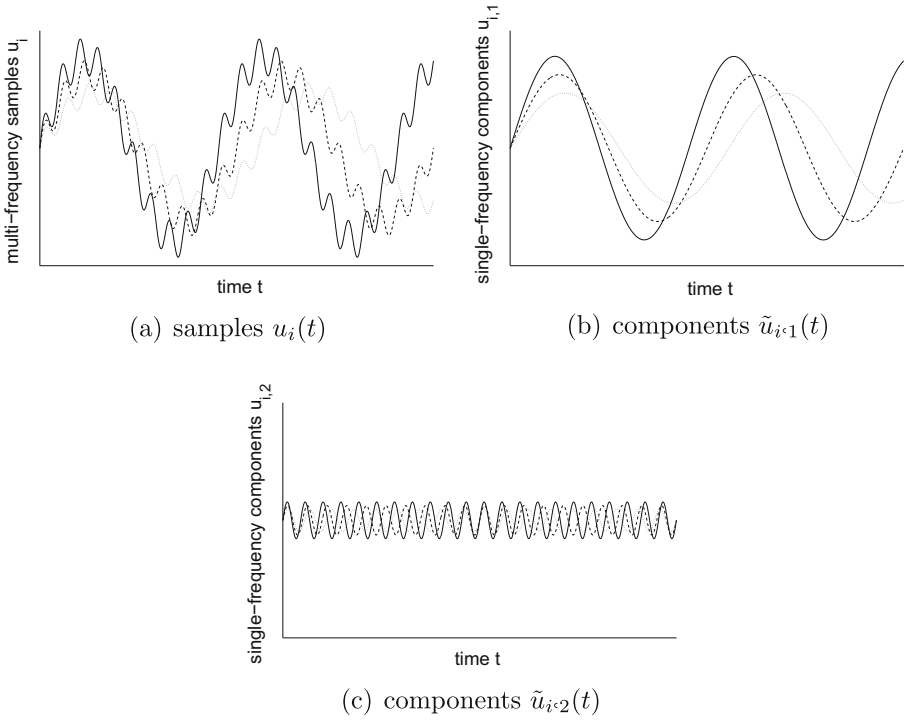

(a) samples $u_i(t)$ (b) components $\tilde{u}_{i,1}(t)$

(c) components $\tilde{u}_{i,2}(t)$

Fig. 1. Decomposition of multi-frequency samples $u_i(t)$ into single-frequency components.

in multi-frequency signals. The nodal description results in multi-frequency responses due to the multiple natural frequencies of the system. The modal description gives rise to multi-frequency signals due to the change of the natural modes and frequencies of the system caused by the coupling with the flow. Multiple harmonics in the dynamical response of structures can also be a result of multi-frequency forcing and structural nonlinearities. The modal decomposition is applicable to linear structures only because it is based upon the structural eigenmodes.

The stochastic response of a continuous structure is analyzed by, firstly, projecting the sampled responses $u_i(t)$ onto either a nodal or modal basis, resulting in multi-frequency signals $u_{i,j}(t)$ with $j = 1,\ldots,N_{\mathrm{DOF}}$ and N_{DOF} the number of degrees-of-freedom of the discretized structure. Secondly, the multi-frequency nodal or modal response signals $u_{i,j}(t)$ are decomposed into their single-frequency components $\tilde{u}_{i,j,k}(t)$, with $k = 1,\ldots,N_{\mathrm{f}}$, using the wavelet analysis based on (2) and (3). UASFE interpolation is then, thirdly, performed for the single-frequency components $\tilde{u}_{i,j,k}(t)$ of the nodal or modal response to obtain $\tilde{u}_{j,k}(t,\omega)$. Finally, the UASFE results for the components $\tilde{u}_{j,k}(t,\omega)$ are summed together

$$u(t,\omega) = \sum_{j=1}^{N_{\mathrm{DOF}}} \sum_{k=1}^{N_{\mathrm{f}}} \tilde{u}_{j,k}(t,\omega), \tag{6}$$

to determine the stochastic response surface $u(t,\omega)$.

2.3. Unsteady Adaptive Stochastic Finite Elements sampling interpolation

The single-frequency signals $\tilde{u}_{i,j,k}(t)$ which result from the wavelet decomposition of multi-frequency signals $u_{i,j}(t)$ are interpolated using Unsteady Adaptive Stochastic Finite Elements (UASFE) with interpolation of the samples at constant phase [36]. The values of the n random parameters $\mathbf{a}(\omega)$ for the N_{s} deterministic computations are selected using a non-intrusive Adaptive Stochastic Finite Elements (ASFE) method based on Newton–Cotes quadrature points in simplex elements [37]. The ASFE formulation employs a piecewise quadratic approximation of the response surface by dividing parameter space A into N_{e} simplex elements A_l with $l = 1,\ldots,N_{\mathrm{e}}$. The quadratic approximation in the elements is constructed by performing deterministic computations for the values of the random parameters $\mathbf{a}(\omega)$ that correspond to the $\binom{n+2}{2}$ second-degree Newton–Cotes quadrature points in the elements shown in the two-dimensional example of Fig. 2(a). The formulation can geometrically be extended to arbitrarily higher-dimensional parameter spaces A.

The single-frequency signals $\tilde{u}_{i,j,k}(t)$ are interpolated at constant phase by scaling them with their phase $\phi_{i,j,k}(t)$ according to

$$\tilde{u}^{*}_{i,j,k}(\phi_{i,j,k}(t)) = \tilde{u}_{i,j,k}(t). \tag{7}$$

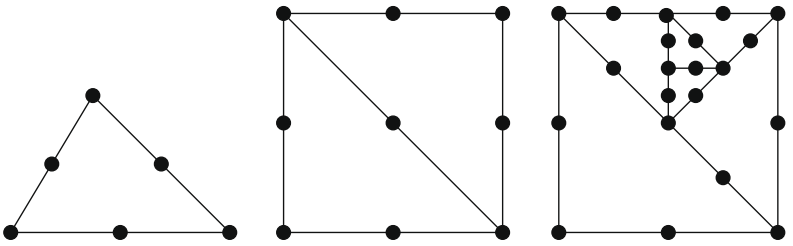

Fig. 2. Discretization of two-dimensional parameter space A using 2-simplex elements and second-degree Newton–Cotes quadrature points given by the dots.

The time series of the phases $\phi_{i,j,k}(t)$ and the scaled signals $\tilde{u}^*_{i,j,k}(\phi_{i,j,k}(t))$ are interpolated using the piecewise quadratic interpolation of ASFE to the functions $\phi_{j,k}(t,\omega)$ and $\tilde{u}^*_{j,k}(\phi_{j,k}(t,\omega),\omega)$, respectively. The result of the ASFE interpolation $\tilde{u}^*_{j,k}(\phi_{j,k}(t,\omega),\omega)$ is scaled back to a function of time $\tilde{u}_{j,k}(t,\omega)$ using

$$\tilde{u}_{j,k}(t,\omega) = \tilde{u}^*_{j,k}(\phi_{j,k}(t,\omega),\omega). \tag{8}$$

The approximation of the stochastic response surface $u(t,\omega)$ is finally obtained by summing the contributions of the single-frequency components $\tilde{u}_{j,k}(t,\omega)$ according to (6).

The phase $\phi_{i,j,k}(t)$ is extracted from the single-frequency signals using a trial-and-error procedure based on the local extrema of the time series $\tilde{u}_{i,j,k}(t)$. The procedure identifies a cycle of oscillation based on two or more successive local maxima. The selected cycle is accepted if the maximal error of its extrapolation in time with respect to the actual sample is smaller than a threshold value $\bar{\varepsilon}_k$ for at least one additional cycle length. The function for the phase $\phi_k(t)$ in the whole time domain $t \in T$ is constructed by identifying all successive cycles of $u_k(t)$ and extrapolation to $t = 0$ and $t = t_{\max}$ before and after the first and last complete cycle, respectively. The phase is normalized to zero at the start of the first cycle and a user-defined parameter determines whether the sample is assumed to attain a local extremum at $t = 0$. The UASFE interpolation is restricted to the time domain that corresponds to the range of phases that is reached by all samples in each of the elements. UASFE can be applied to problems in which the phase of the single-frequency signals $\tilde{u}_{i,j,k}(t)$ is well-defined. In other cases the ASFE interpolation is applied directly to the samples $u_i(t)$.

The initial discretization of parameter space A consisting of the minimum of $N_{e_{ini}} = n!$ simplex elements and $N_{s_{ini}} = 3^n$ samples, see Fig. 2(b), is adaptively refined as illustrated in Fig. 2(c). The refinement measure ρ_l in element A_l is defined as

$$\rho_l = P_l V_l^{N_V} \max(|\mathrm{eig}_1(H_l(u))|, \ldots, |\mathrm{eig}_n(H_l(u))|), \tag{9}$$

based on the total of the maximum absolute eigenvalues of the Hessian H_l

$$H(y(x_1,\ldots,x_n)) = \begin{bmatrix} \frac{\partial^2 y}{\partial x_1^2} & \frac{\partial^2 y}{\partial x_1 \partial x_2} & \cdots & \frac{\partial^2 y}{\partial x \partial x_n} \\ \frac{\partial^2 y}{\partial x_2 \partial x_1} & \frac{\partial^2 y}{\partial x_2^2} & \cdots & \frac{\partial^2 y}{\partial x_2 \partial x_n} \\ \vdots & \vdots & \ddots & \vdots \\ \frac{\partial^2 y}{\partial x_n \partial x_1} & \frac{\partial^2 y}{\partial x_n \partial x_2} & \cdots & \frac{\partial^2 y}{\partial x_n^2} \end{bmatrix}, \tag{10}$$

of $\phi_{j,k}(t,\omega)$ and $\tilde{u}^*_{j,k}(\phi_{j,k}(t,\omega),\omega)$ for $j = 1,\ldots,N_{\mathrm{DOF}}$ and $k = 1,\ldots,N_{\mathrm{f}}$. The refinement measure ρ_l is weighted by the probability contained by element A_l defined by the volume of the element Ω_l is probability space Ω

$$P_l = \frac{1}{n!} |\det(\, \omega_{l,0} - \omega_{l,1} \quad \omega_{l,1} - \omega_{l,2} \quad \cdots \quad \omega_{l,n-1} - \omega_{l,n} \,)|, \tag{11}$$

and scaled by the factor $N_V = 2$ to compensate the increase of the second-order derivatives of the quadratic approximation with the decrease of the element volumes

$$V_l = \frac{1}{n!} |\det(\, a_{l,0} - a_{l,1} \quad a_{l,1} - a_{l,2} \quad \cdots \quad a_{l,n-1} - a_{l,n} \,)|, \tag{12}$$

containing a discontinuity, where $a_{l,j}$ are the $n+1$ vertices of the n-simplex A_l in parameter space A, and $\omega_{l,j}$ are given by the mapping of $a_{l,j}$ to probability space Ω for $j = 0,\ldots,n$. Stochastic grid refinement is terminated when the convergence measure δ_{N_e} for the mean $\mu_u(t)$ and standard deviation $\sigma_u(t)$ defined as in [35]

$$\delta_{N_e} = \max\left(\frac{|\mu_{u_{\lfloor N_e/2 \rfloor}}(t) - \mu_{u_{N_e}}(t)|_\infty}{|\mu_{u_{N_e}}(t)|_\infty}, \frac{|\sigma_{u_{\lfloor N_e/2 \rfloor}}(t) - \sigma_{u_{N_e}}(t)|_\infty}{|\sigma_{u_{N_e}}(t)|_\infty} \right), \tag{13}$$

is smaller than a user-defined stopping criterion $\bar{\delta}$ or when a threshold for the maximum number of samples $\overline{N}_s$ is exceeded. Convergence measure δ_{N_e} can be extended to include higher-order moments.

Due to the location of the Newton–Cotes quadrature points the required number of deterministic computations is relatively low, since the deterministic samples are reused in successive refinements and the samples are used in approximating the response in multiple elements. In order to preserve monotonicity and extrema of the samples the elements are subdivided into $N_{e_{lin}} = 2^n$ subelements with a linear approximation of the response where necessary without performing additional deterministic. This formulation conserves the total variation of the samples and is, therefore, total variation diminishing (TVD) [15] in probability space. This prevents unphysical predictions due to overshoots and undershoots near singularities at the expense that the method does not achieve spectral convergence for smooth responses as Galerkin and Gauss quadrature Stochastic Finite Elements methods can.

As is common in multi-element methods, the probability of the random parameters $\mathbf{a}(\omega)$ is assumed to be zero outside a finite domain. Probability distributions on infinite domains are truncated at a small enough threshold value for the probability, such that the truncation error is small compared to other numerical errors that occur in practical applications. The interpolation of the single-frequency components at constant phase can also be performed using another non-intrusive uncertainty quantification scheme than the ASFE interpolation employed here.

2.4. Algorithm summary

The resulting Unsteady Adaptive Stochastic Finite Elements algorithm for resolving the effect of random parameters on fluid–structure interaction systems with multi-frequency responses and continuous structures is listed below:

1. Compute the deterministic system responses $u_i(t)$ by solving (1) for the parameter values $\mathbf{a}_i$ corresponding to the quadrature points in the initial stochastic grid for $i = 1, \ldots, N_{s_{ini}}$.
2. Project the deterministic responses of the continuous structure onto a nodal finite element representation or onto the natural modes of the structure in vacuum, which results in the time series $u_{i,j}(t)$ with $j = 1, \ldots, N_{DOF}$.
3. Decompose the multi-frequency signals $u_{i,j}(t)$ into single-frequency components $\tilde{u}_{i,j,k}(t)$ using wavelet decomposition based on Eqs. (2) and (3).
4. Interpolate the single-frequency time series $\tilde{u}_{i,j,k}(t)$ to the functions $\tilde{u}_{j,k}(t,\omega)$ using UASFE interpolation of the signals $\tilde{u}_{i,j,k}(t)$ at constant phase.
5. Determine the stochastic response surface $u(t,\omega)$ by summing the contributions of the single-frequency components $\tilde{u}_{j,k}(t,\omega)$ according to Eq. (6).
6. Refine the element of the stochastic grid with the largest value of refinement measure ρ_l with $l = 1, \ldots, N_{e_{ini}}$.
7. Repeat steps 1–6 for the parameter values $\mathbf{a}_i$ corresponding to the new quadrature points in the refined element with $i = N_{s_{old}} + 1, \ldots, N_{s_{new}}$.
8. Stop the adaptive stochastic grid refinement based on convergence of the mean $\mu_u(t)$ and standard deviation $\sigma_u(t)$, or threshold $\overline{N}_s$ for the maximum number of samples.

For single-degree-of-freedom structural systems step 2 can obviously be omitted.

3. Results

The UASFE method is applied to multi-frequency signals and continuous structures in a harmonically forced oscillator in Section 3.1, a flutter panel in Section 3.2, and the transonic three-dimensional AGARD 445.6 wing in Section 3.3. The results are compared to those of converged Monte Carlo simulations with uniformly sampled realizations in sample space $\omega \in [0,1]^{N_s}$.

3.1. Harmonically forced oscillator

The mass–spring system with a harmonic forcing as described in Section 3.1.1 is a simple model problem for a structural system with aerodynamic forcing. The resulting multi-frequency response contains the forcing frequency and the natural frequency of the structure. The effect of a random spring stiffness on the multi-frequency response is resolved in Section 3.1.2. In Section 3.1.3 the effect of independent randomness in a combination of spring stiffness and forcing frequency is studied.

3.1.1. Forced mass–spring system

The forced mass–spring system of Fig. 3 is governed by

$$M\frac{\partial^2 x}{\partial t^2} + K(\omega)x = A_F \sin \omega_F(\omega)t, \quad t \in [0,\infty), \tag{14}$$

with initial conditions $x(0) = 0$ and $\partial x/\partial t(0) = 0$ for the position and velocity of mass $M = 1$, and forcing amplitude $A_F = 1$. Randomness is assumed in the positive parameters spring stiffness $K(\omega)$ and forcing frequency $\omega_F(\omega)$ given by truncated

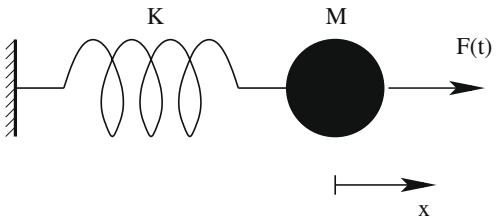

Fig. 3. Forced mass–spring system.

lognormal distributions with mean values $\mu_K = 1$ and $\mu_{\omega_F} = 5$ and coefficients of variation of 10%. The forcing frequency ω_F has been chosen here to differ sufficiently from the structural eigenfrequency for the mean structural stiffness $\sqrt{\mu_K/M} = 1$ for the wavelet decomposition to be effective. The tails of the probability distribution are truncated such that the resolved parameter domain accounts for 99.8% of the realizations as is common for multi-element methods. The resulting 0.2% truncation error is small compared to the usual discretization and time integration errors in engineering simulations. The $N_f = 2$ frequencies in the time evolution of $x(t,\omega)$ can clearly be recognized in the analytical solution of (14)

$$x(t,\omega) = \frac{A_F}{K(\omega) - M\omega_F(\omega)^2}\left(\sin\omega_F(\omega)t - \frac{\omega_F(\omega)}{\sqrt{K(\omega)/M}}\sin\sqrt{\frac{K(\omega)}{M}}t\right). \tag{15}$$

The frequency of the first sinusoidal term equals the forcing frequency ω_F and the second term is governed by the natural frequency of the structure $\sqrt{K(\omega)/M}$. Analytical solution (15) is evaluated at discrete time levels $t_m = m\Delta t$, with $m = 0,\ldots,N_t$, $N_t = t_{max}/\Delta t$, and $\Delta t = 0.01$ for the results to be comparable with those of problems solved by numerical time integration. Since each sample reaches a different minimum and maximum phase in the time domain $t \in T$, the ASFE interpolation at constant phase is restricted to the range of phases that is reached by all samples in an element. The UASFE-cp interpolation is then limited to the time domain which corresponds to $\tilde{\phi} \in [\max_k \phi_k(0), \min_k \phi_k(t_{max})]$ in the elements. Therefore, the samples are computed until $t_{max} = 100$ to determine the stochastic solution until $t = 50$. The considered time interval corresponds to approximately 80 and 16 periods for the mean harmonic forcing frequency μ_{ω_F} and the structural eigenfrequency for the mean value of the stiffness μ_K, respectively.

3.1.2. Multi-frequency response resolved

First randomness is assumed in the spring stiffness $K(\omega)$ in combination with the mean value of the forcing frequency μ_{ω_F}. According to analytical solution (15), $K(\omega)$ influences the frequency and amplitude of the second sinusoidal term originating from the eigenmotion of the structure. The randomness has no effect on the frequency and only a small effect on the amplitude of the term induced by the forcing. These observations are illustrated by the $N_s = 3$ samples of the initial UASFE discretization of probability space with $N_e = 1$ element for $t = [0,20]$ in Fig. 4(a). The multi-frequency responses consist of a varying large amplitude and low-frequency eigenmotion superimposed with a small amplitude and constant forcing frequency signal. It is essential to decompose these multi-frequency signals into single-frequency components, since the phase of the samples is determined by the UASFE algorithm by identifying periods of oscillation based on the continuation of the signal after a local maximum.

The separate frequency components can be recognized in the level 7 wavelet decomposition of the samples $x_i(t)$ into two single-frequency signals $\tilde{x}_{i,k}(t)$ shown in Fig. 4(b) and (c). It can be seen that the wavelet decomposition does not exactly reconstruct the single-frequency components as periodic sinusoidal functions. This results in a slightly different decomposition of each sample, which can affect the convergence behavior of the method. These effects decrease as the difference between the frequencies increases. The UASFE interpolation of the samples is performed at constant phase ϕ after extracting the phase as function of time $\phi_{i,k}(t)$ from the single-frequency signals $\tilde{x}_{i,k}(t)$. In Fig. 4(d) the single-frequency signals as function of their phase $\tilde{x}^*_{i,k}(\phi_{i,1})$ are shown for $j = 1$. It can be observed that scaling the signals $\tilde{x}_{i,k}(t)$ with their phase $\phi_{i,k}(t)$ eliminates the effect of the increasing phase differences with time, which results in the time-independent accuracy of UASFE. For $j = 2$ the plot of the single-frequency signals in terms of their phase $\tilde{x}^*_{i,2}(\phi_{i,2})$ resembles that of the time histories $\tilde{x}_{i,2}(t)$ of Fig. 4(c), since their frequency is not affected by the randomness in $K(\omega)$.

The component phases $\phi_{i,k}(t)$ are shown in Fig. 5. The different frequencies of the samples $\tilde{x}_{i,1}(t)$ result a linear increase in time of the phase differences between the sampled phases $\phi_{i,1}(t)$. Since $K(\omega)$ has no effect on the frequency of $\tilde{x}_{i,2}(t)$ the evolution of the phases $\phi_{i,2}(t)$ is virtually identical.

Combining the UASFE interpolations of the decomposed single-frequency components $\tilde{x}_k(t,\omega)$ according to (5) results in the approximation of the mean $\mu_x(t)$ and standard deviation $\sigma_x(t)$ given in Fig. 6 for $N_e = 1$ and $N_s = 3$. The results match those of a converged Monte Carlo simulation with $N_s = 1000$ samples up to a maximum error of $\varepsilon = 3.4 \times 10^{-2}$, while reducing the computational costs in terms of the number of deterministic computations by three orders of magnitude. The error ε is computed using resampling of the piecewise polynomial response surface in the Monte Carlo sampling points. It therefore reflects the residual error in $\mu_x(t)$ and $\sigma_x(t)$ due to the response surface approximation with respect to the Monte Carlo simulation. This is a common approach to account for the confidence level of the finite Monte Carlo sample size.

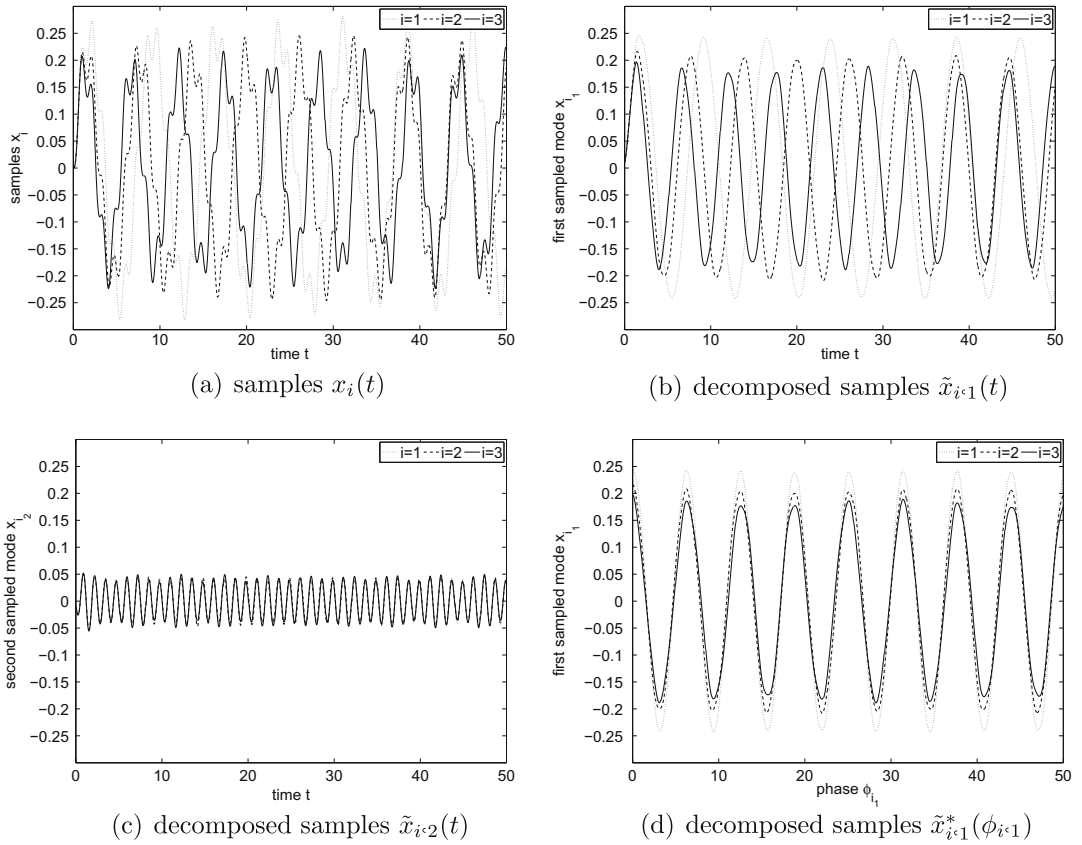

(a) samples $x_i(t)$ (b) decomposed samples $\tilde{x}_{i\text{‹}1}(t)$

(c) decomposed samples $\tilde{x}_{i\text{‹}2}(t)$ (d) decomposed samples $\tilde{x}^*_{i\text{‹}1}(\phi_{i\text{‹}1})$

Fig. 4. The $N_s = 3$ samples of UASFE with $N_e = 1$ element for the harmonically forced oscillator with random $K(\omega)$.

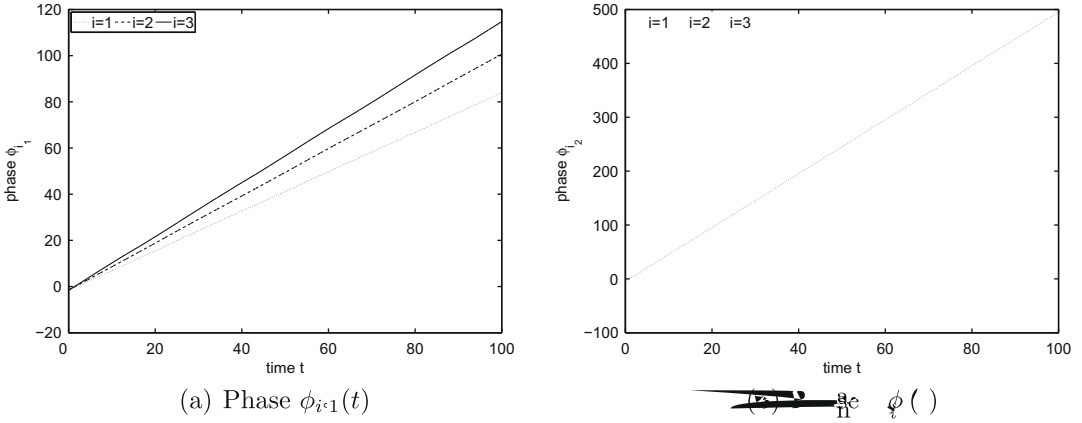

(a) Phase $\phi_{i\text{‹}1}(t)$

Fig. 5. Phase of the $N_s = 3$ decomposed samples $\tilde{x}^*_{i,k}(\phi_{i,k})$ of UASFE with $N_e = 1$ element for the harmonically forced oscillator with random $K(\omega)$.

In the time history of the mean $\mu_x(t)$ the two frequency components are clearly present in terms of a decaying low-frequency oscillation superimposed by a high-frequency periodic oscillation. The low-frequency component with approximately the natural frequency of the structure decays due the effect of $K(\omega)$ on the frequency and the increasing phase differences between the low-frequency components of the samples $\tilde{x}_{i,1}(t)$. The high-frequency forcing component of $\mu_x(t)$ does not decay with time, since the forcing frequency is unaffected by $K(\omega)$. The mean of this stochastic multi-frequency response does, therefore, not reach an asymptotically steady value, in contrast with single-frequency periodic responses subject to a random frequency.

The standard deviation $\sigma_x(t)$ shows, on the other hand, the typical behavior of single-frequency signal with a random frequency and deterministic initial condition. The initially oscillatory increase to a steady asymptotic value of $\sigma_x = 0.148$

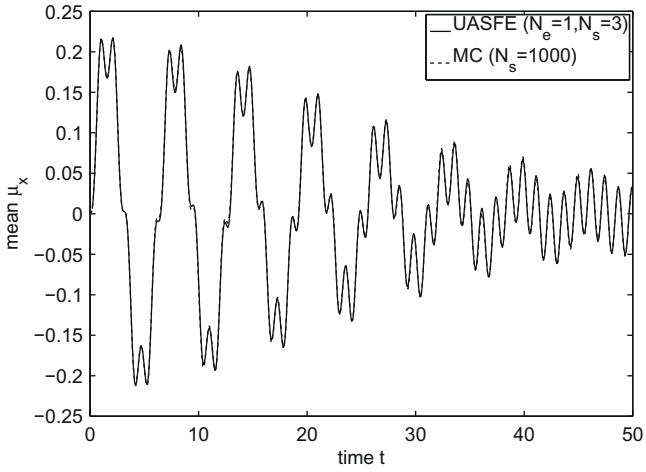

(a) mean $\mu_x(t)$

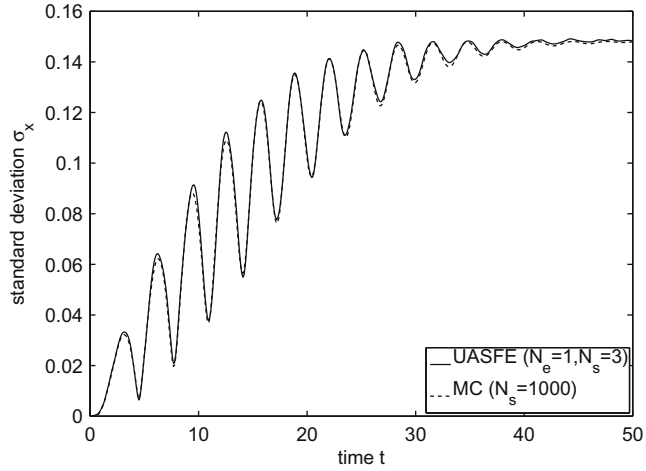

(b) standard deviation $\sigma_x(t)$

Fig. 6. Results for the harmonically forced oscillator with random $K(\omega)$.

originates from the effect of $K(\omega)$ on the frequency and amplitude of the eigenmotion component of the response $\tilde{x}_{i,1}(t)$. The forcing component $\tilde{x}_{i,1}(t)$ does not significantly contribute to $\sigma_x(t)$, since $K(\omega)$ has only a small effect on the amplitude on the forcing mode.

In Fig. 7 the error convergence of UASFE based on the components of analytical solution (15) is given. The relative maximum error in the mean $\mu_x(t)$ and standard deviation $\sigma_x(t)$ with respect to the Monte Carlo reference solution are shown. The UASFE discretization maintains asymptotically a fourth-order error convergence also for multi-frequency responses, which is in accordance with the underlying fourth-order second-degree Newton–Cotes quadrature rule.

3.1.3. Combination of randomness in structure and forcing

Randomness in an independent combination of spring stiffness $K(\omega)$ and forcing frequency $\omega_F(\omega)$ results in a qualitatively different stochastic solution. The UASFE approximation of the mean $\mu_x(t)$ and standard deviation $\sigma_x(t)$ for $N_e = 4$ elements and $N_s = 13$ given in Fig. 8 is converged up to $\delta_{N_e} = 5 \times 10^{-2}$. The comparison with a converged Monte Carlo result based on $N_s = 6.3 \times 10^4$ samples shows that UASFE leads to a maximum error of $\varepsilon = 1.5 \times 10^{-2}$ while achieving a reduction of samples by three orders of magnitude. The large sample size required by the Monte Carlo method to converge illustrates the complexity of this multi-scale stochastic example. The mean $\mu_x(t)$ shows for this case a decaying oscillation to zero due to the effect of $K(\omega)$ and $\omega_F(\omega)$ on the frequency of both modes $\tilde{x}_{i,1}(t)$ and $\tilde{x}_{i,2}(t)$. The contribution of the high-frequency component $\tilde{x}_{i,2}(t)$ to $\mu_x(t)$ decays fast and can only be identified for $t < 5$. The standard deviation $\sigma_x(t)$ shows a more complex initial behavior due to the additional randomness in $\omega_F(\omega)$. For $t > 5$ the standard deviation $\sigma_x(t)$ is slightly higher compared to the results for deterministic forcing with an asymptotic value of $\sigma_x = 0.154$.

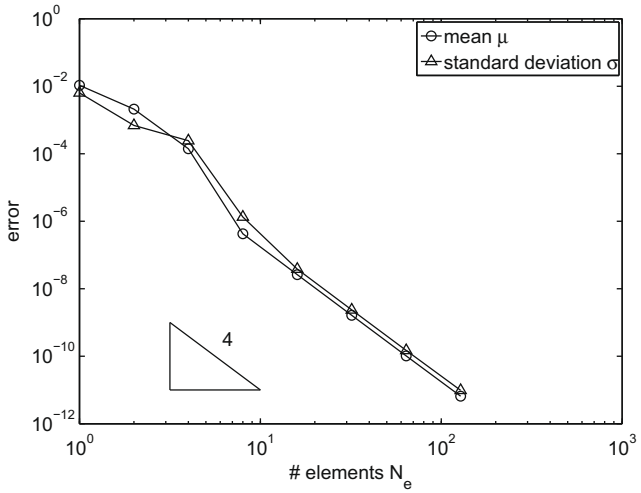

Fig. 7. UASFE error convergence for the harmonically forced oscillator with random $K(\omega)$.

3.2. Flutter panel

The two-dimensional panel problem is a relatively simple example of a continuous structure which exhibits a multi-frequency response as a result of aerodynamic loads. A modal representation of the response of the panel problem described in Section 3.2.1 is used here in terms of the eigenmodes of the structure. The effect of randomness in the panel density on the energy of the structure is analyzed in Section 3.2.2. In Section 3.2.3 a random field for the modulus of elasticity of the plate is considered.

3.2.1. Panel problem

The dynamical behavior of a fully clamped plate subject to a supersonic flow sketched in Fig. 9 is a standard test problem in aeroelasticity [12,29]. The material of the plate with length $L = 1$ m has a Poisson ratio of $\nu_p = 0.35$. The air flow with unperturbed density $\rho_\infty = 1.225\ \mathrm{kg/m^3}$ and pressure $p_\infty = 1.0 \times 10^5$ Pa has a free stream Mach number of $M_\infty = 2.5$ and ratio of specific heats $\gamma = 1.4$. The effect of randomness in the density ρ_p and the modulus of elasticity $E_p(x,\omega)$ of the plate is considered. Parametric randomness is assumed in the plate density ρ_p given by a uniform distribution around mean $\mu_{\rho_p} = 2700\ \mathrm{kg/m^3}$ with coefficient of variation cv_{ρ_p} of 10%. The randomness in the modulus of elasticity of the plate $E_p(x,\omega)$ is described in terms of a Gaussian random field with local mean $\mu_E = 70 \times 10^9$ Pa and local coefficient of variation of 0.1% for the linear physical modeling to remain valid. The spatial correlation is given by the exponential covariance function

$$C(x_1, x_2) = \mathrm{e}^{-\frac{|x_1 - x_2|}{L_c}}, \tag{16}$$

with correlation length $L_c = L$ equal the characteristic length of the plate L. This will also result in an efficient expansion of the correlation in Karhunen–Loève terms, since it is well known that the Karhunen–Loève expansion is less effective for weakly correlated data [21]. The thickness of the plate $h = 4.38 \times 10^{-3}$ m is chosen such that it corresponds to the deterministic flutter point.

The equations of motion of the plate are discretized by a finite element discretization with three spatial elements with Hermitian basis functions for the nodal displacements and rotations. Piston theory is used to determine the aerodynamic pressure $p_u(x,t,\omega)$ on the upper side of the panel

$$p_u(x,t,\omega) = \rho_\infty c_\infty \left(\frac{\partial w}{\partial t} + V_\infty \frac{\partial w}{\partial x} \right), \tag{17}$$

with vertical plate displacement $w(x,t,\omega)$, and free stream speed of sound c_∞ and velocity V_∞. First-order relation (17) is a valid approximation for supersonic flow with Mach numbers from 2 to 5 [12]. The discretization of the flow and the structure results in a matrix equation governing the coupled aeroelastic system

$$M \frac{\partial^2 u}{\partial t^2} + D \frac{\partial u}{\partial t} + K u = 0, \tag{18}$$

with $u(t,\omega)$ the nodal degrees of freedom of the structure, structural mass matrix M, aerodynamic damping matrix D, and stiffness matrix K with a symmetric and asymmetric contribution of the structure and the flow, respectively. The random field for the modulus of elasticity $E_p(x,\omega)$ is discretized in terms of a finite number of random parameters using a Karhun-

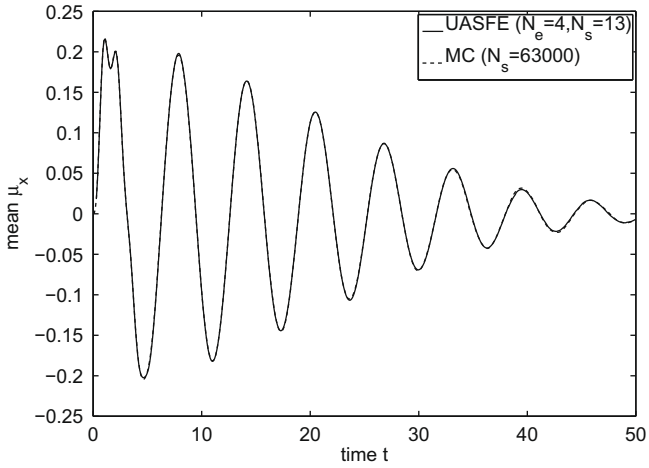

(a) mean $\mu_x(t)$

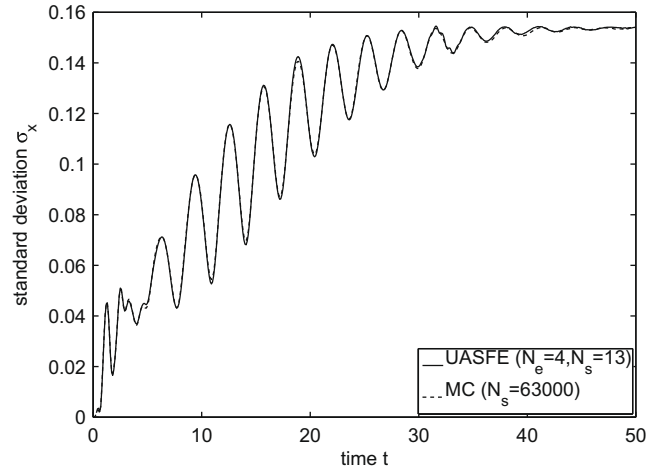

(b) standard deviation $\sigma_x(t)$

Fig. 8. Results for the harmonically forced oscillator with random $K(\omega)$ and $\omega_f(\omega)$.

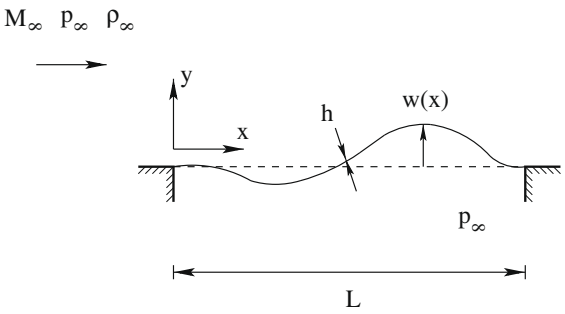

Fig. 9. Two-dimensional flutter panel problem.

en–Loève (KL) expansion [21] truncated after the second term. Time marching is performed until $t = 0.5$ using a second-order implicit time integration scheme with a time step of $\Delta t = 1 \times 10^{-4}$.

Since the aerodynamic forces are modeled here using linear piston theory, the eigenfrequencies and eigenmodes of the coupled fluid–structure system can, in principle, be determined. However, this example is used here as a test problem for an aeroelastic system with, in general, nonlinear aerodynamics. It is, therefore, assumed in the stochastic analysis that only

the eigenmodes of the linear structure in vacuum are known. The motion of the structure is here described in terms of the structural eigenmodes. The initial condition is given by the first eigenmode of the plate with a maximum deflection of 0.01 m.

3.2.2. Continuous structure analyzed

The difference between the eigenmodes of the structure and those of the coupled fluid–structure interaction system for the mean values of the random parameters are shown in Fig. 10 for the $M^{-1}K$ matrix. Due to these differences the initial deflection of the first structural eigenmode excites all eigenmodes of the coupled system. In the resulting dynamical response the coupled eigenmodes oscillate at their coupled eigenfrequencies, which differ from the structural natural frequencies as given in Table 1 for the $M^{-1}K$ matrix. Projecting the plate motion back onto the structural eigenmodes results in multi-frequency signals for the dynamical behavior of the plate described in terms of its structural eigenmodes. Also a nodal description of the structure in terms of the degrees-of-freedom of the finite element discretization gives rise to multi-frequency signals.

The multi-frequency response of the structural eigenmodes is illustrated in Fig. 11 for the example of the velocity component of the fourth eigenmode $v_4(t)$ for randomness in the plate density $\rho_p(\omega)$ and a deterministic modulus of elasticity $E_p = \mu_{E_p}$. The $N_s = 3$ UASFE samples $v_{4_i}(t)$ for $N_e = 1$ element show the effect of the randomness on the multi-frequency response up to $t = 0.1$ s. The multi-frequency signals for the eigenmode deflections and velocities are here decomposed into single-frequency signals using a level 5 wavelet decomposition.

The influence of the random $\rho_p(\omega)$ on the mean $\mu(t)$ and standard deviation $\sigma(t)$ of the total energy of the structure is given in Fig. 12. Also shown are the potential and kinetic energy, $U(t,\omega)$ and $T(t,\omega)$, of the plate defined as

$$U(t,\omega) = \int_0^L \frac{1}{2}\frac{h^3}{12}E_p(x,\omega)\left(\frac{\partial^2 w}{\partial x^2}\right)^2 dx, \tag{19}$$

$$T(t,\omega) = \int_0^L \frac{1}{2}\rho_p(\omega)h\left(\frac{\partial w}{\partial x}\right)^2 dx. \tag{20}$$

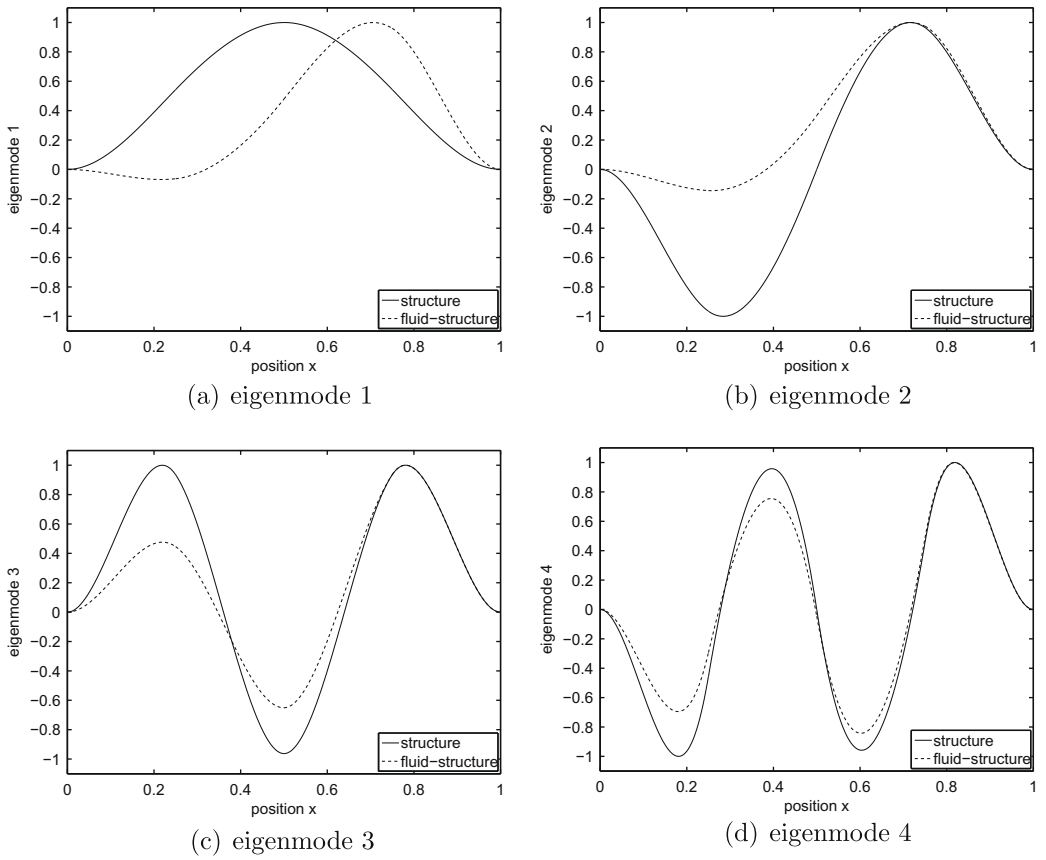

Fig. 10. Deterministic eigenmodes of the structure and the coupled fluid–structure interaction system for the $M^{-1}K$ matrix in the panel problem.

Table 1
Deterministic eigenfrequencies of the structure and the coupled fluid–structure interaction system for the $M^{-1}K$ matrix in the panel problem.

Eigenmode	Eigenfrequency (Hz)	
	Structure	Fluid–structure
1	24.49	53.81
2	68.05	59.78
3	135.0	133.3
4	255.4	254.8

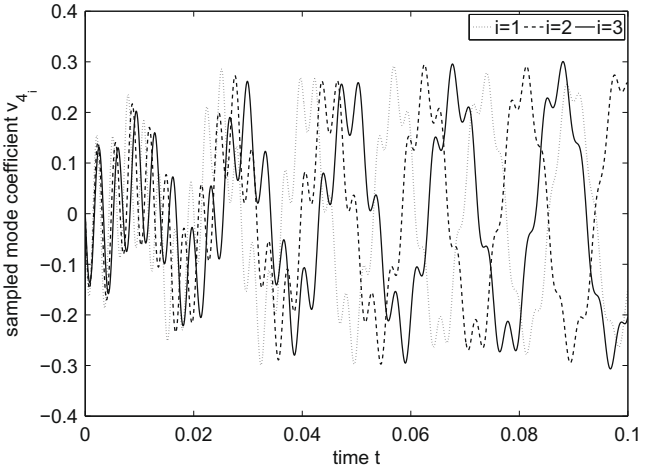

Fig. 11. The $N_s = 3$ sampled velocity components of the fourth eigenmode $v_{4_i}(t)$ of UASFE with $N_e = 1$ element for the panel problem with random plate density $\rho_p(\omega)$.

The UASFE results for $N_e = 1$ element and $N_s = 3$ samples agree up to a maximum error of $\varepsilon = 7.7 \times 10^{-3}$ with converged Monte Carlo results based on $N_s = 500$ samples, while reducing the computational costs by two orders of magnitude. In Fig. 12(a) also the deterministic total structural energy is shown, which exhibits initially a fast increase due to transport of energy from the flow to the structure. The asymptotically periodic oscillation for the total structural energy illustrates that the deterministic parameter settings correspond to the deterministic flutter point. The mean total energy is initially close to the deterministic result for $t < 0.05$. However, for larger t the random $\rho_p(\omega)$ results in an asymptotically diverging mean total energy. This observation is in correspondence with the well know fact that random realizations of an uncertain parameter can lead to unstable behavior of aeroelastic systems. The mean total energy is approximately equally divided between mean potential and kinetic energy.

Random $\rho_p(\omega)$ results also in an increasing standard deviation for the total, potential, and kinetic energy of the plate as shown in Fig. 12(b). Initially the variation of the potential and kinetic energy partially cancel each other, which results in a smaller standard deviation for the total energy. For $t > 0.3$ the standard deviation of the total energy is larger than those of the potential and kinetic energy. The coefficient of variation of the total energy increases to a value of 62.5% at $t = 0.4$, which corresponds to an amplification factor of the input randomness of 6.25.

3.2.3. Random field for modulus of elasticity

The random field for the modulus of elasticity $E_p(x,\omega)$ results in a different behavior of the mean and standard deviation of the potential and kinetic energy, $U(t,\omega)$ and $T(t,\omega)$, of the plate than random $\rho_p(\omega)$, see Fig. 13. Variations in the plate density affect both the frequency and the damping of the aeroelastic system, since $\rho_p(\omega)$ appears in the mass matrix M as a multiplication factor for the matrix entries. On the other hand the random $E_p(x,\omega)$ only influences the amplitude significantly through the symmetric part of the elasticity matrix K. Since the elasticity has a small effect on the frequency of oscillation, all samples of $U(t,\omega)$ and $T(t,\omega)$ oscillate in phase with the deterministic frequency of the system between zero and the different sampled total energies. As a result, the mean and the standard deviation of $U(t,\omega)$ and $T(t,\omega)$ also oscillate alternately between zero and the value of the mean and standard deviation of the total energy, respectively.

The 0.1% variation in the modulus of elasticity has, however, a similar quantitative influence on the mean and standard deviation of the total energy of the plate as the 10% variation of $\rho_p(\omega)$. The total energy of the plate is, therefore, two orders of magnitude more sensitive to variation in $E(x,\omega)$ than in $\rho_p(\omega)$. The mean and standard deviation increase in time to a coefficient of variation of 48.5% at $t = 0.4$, which corresponds to an amplification factor for the coefficient of variation of 485.

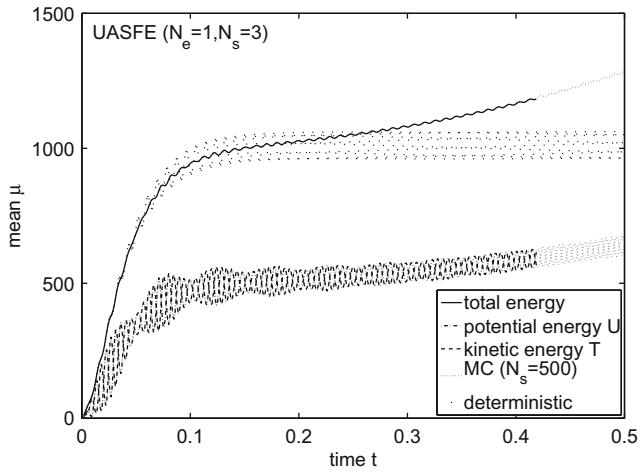

(a) mean $\mu(t)$

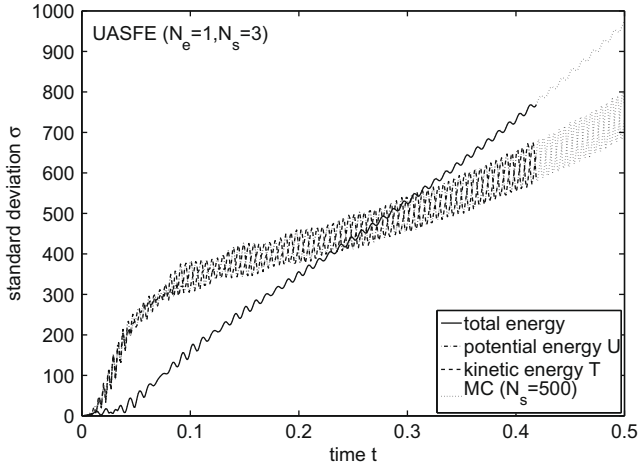

(b) standard deviation $\sigma(t)$

Fig. 12. Results for the panel problem with random plate density $\rho_p(\omega)$.

The UASFE results shown for $N_e = 8$ elements and $N_s = 25$ samples are converged up to 1×10^{-3}. In Fig. 14 the mean and standard deviation of the total energy approximation of UASFE are compared to those of Monte Carlo simulation based on the same Karhunen–Loève expansion as used for UASFE to eliminate the Karhunen–Loève discretization error. The Monte Carlo results for 10^3, 10^4, and 10^5 samples converge to the UASFE results, although Monte Carlo simulation with 10^5 samples has not yet reached the accuracy of UASFE based on $N_s = 25$ samples. The comparison for the potential and kinetic energy results in the same observations.

3.3. Three-dimensional transonic wing

The transonic AGARD 445.6 wing [40] is a standard benchmark case for the fluid–structure interaction of a three-dimensional continuous structure. The discretization of the aeroelastic configuration is described in Section 3.3.1. In Section 3.3.2 randomness is introduced in the free stream velocity. The stochastic response of the system and the flutter probability are determined.

3.3.1. AGARD 445.6 wing benchmark problem

The AGARD aeroelastic wing configuration number 3 [40] known as the weakened model is considered here with a NACA 65A004 symmetric airfoil, taper ratio of 0.66, 45° quarter-chord sweep angle, and a 2.5-foot semi-span subject to an inviscid flow. The structure is described by a nodal discretization using an undamped linear finite element model in the *Matlab* finite element toolbox *OpenFEM* [25]. The discretization contains in the chordal and spanwise direction 6×6 brick-elements with 20 nodes and 60 degrees-of-freedom, and at the leading and trailing edge 2×6 pentahedral elements with 15 nodes and 45

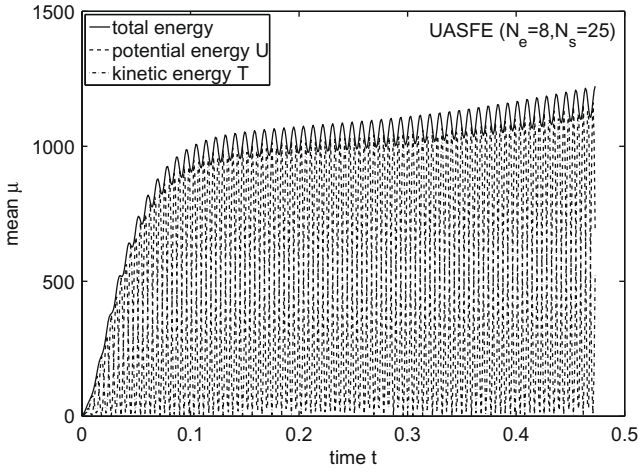

(a) mean $\mu(t)$

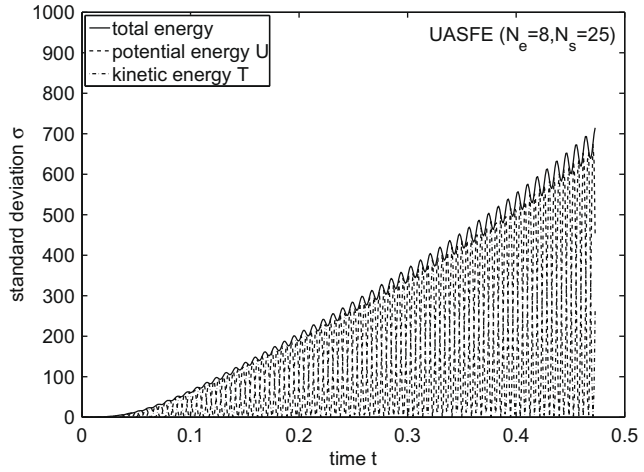

(b) standard deviation $\sigma(t)$

Fig. 13. Results for the panel problem with random modulus of elasticity field $E(x,\omega)$.

degrees-of-freedom as in [43]. The orthotropic material properties are obtained from [3] and the fiber orientation is taken parallel to the quarter-chord line.

The Euler equations for inviscid flow [7] are solved using a second-order central finite volume discretization on a $60 \times 15 \times 30$ m domain using an unstructured hexahedral mesh. The free stream conditions for the density $\rho_\infty = 0.099468$ kg/m^3 and pressure $p_\infty = 7704.05$ Pa are taken from [40]. Time integration of the samples is performed using a third-order implicit Runge–Kutta scheme [17] until $t = 1.25$ s to determine the stochastic solution until $t = 1$ s. The first bending mode with a vertical tip displacement of $y_{\text{tip}} = 0.01$ m is used as initial condition for the structure, see Fig. 15. The initial conditions of the flow are equal to the free stream boundary conditions.

The coupled fluid–structure interaction system is solved using a partitioned IMEX scheme [41,42] with explicit treatment of the coupling terms without sub-iterations. An Arbitrary Lagrangian–Eulerian formulation is employed to couple the fluid mesh with the movement of the structure. The flow forces and the structural displacements are imposed on the structure and the flow using nearest neighbor and radial basis function interpolation [43], respectively. The fluid mesh is also deformed using radial basis function interpolation of the boundary displacements [5]. A convergence study has been performed to determine a suitable flow mesh discretization and time step size. Deterministic results for the selected flow mesh with 3.1×10^4 volumes and time step of $\Delta t = 2.5 \times 10^{-3}$ s agree well with experimental and computational results in literature [18,40,43]. The deterministic flutter velocity is found to be $U_{\text{flut}} = 313$ m/s, which corresponds to a Mach number of $M_\infty = 0.951$.

3.3.2. Randomness causes non-zero flutter probability

In the following, the effect of randomness in the free stream velocity $U_\infty(\omega)$ is studied. The mean free stream velocity is chosen 5% below the actual deterministic flutter velocity, $\mu_{U_\infty} = 0.95 U_{\text{flut}}$, to assess the effectiveness of a realistic design

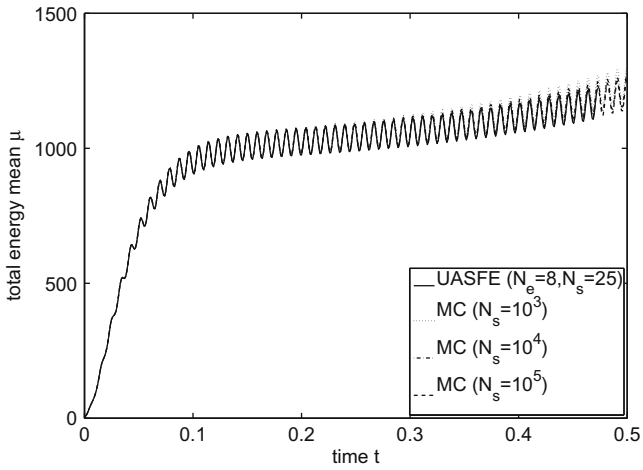

(a) mean $\mu(t)$

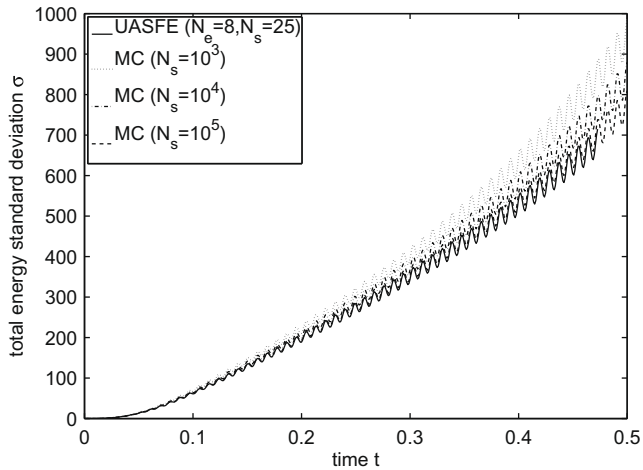

(b) standard deviation $\sigma(t)$

Fig. 14. Results for the panel problem with random modulus of elasticity field $E(x, \omega)$.

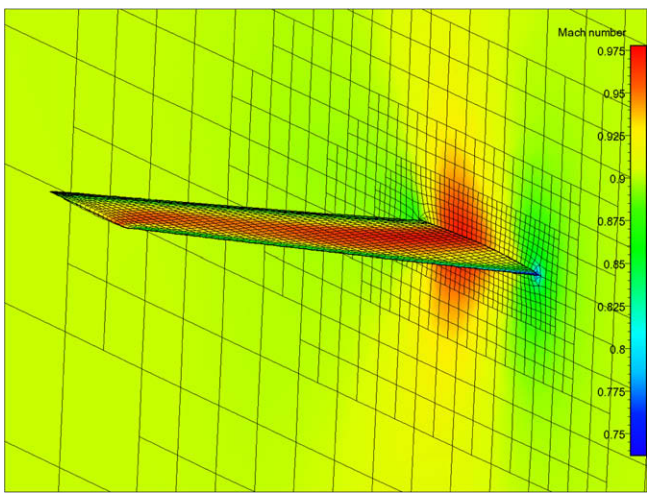

Fig. 15. Initial condition and grid for the AGARD 445.6 wing for mean free stream velocity μ_{U_∞}.

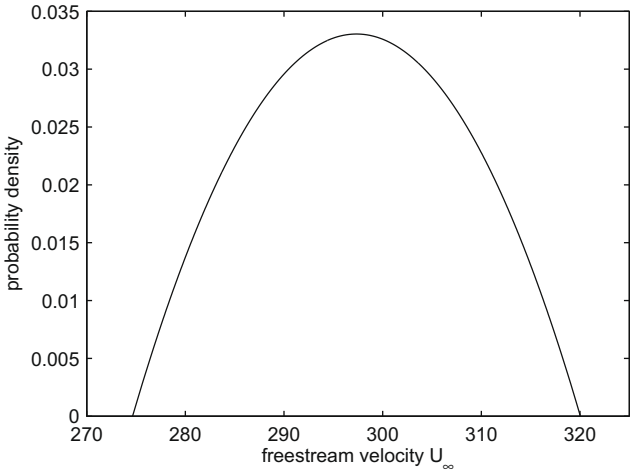

Fig. 16. Input probability density function of the freestream velocity U_∞ for the AGARD 445.6 wing.

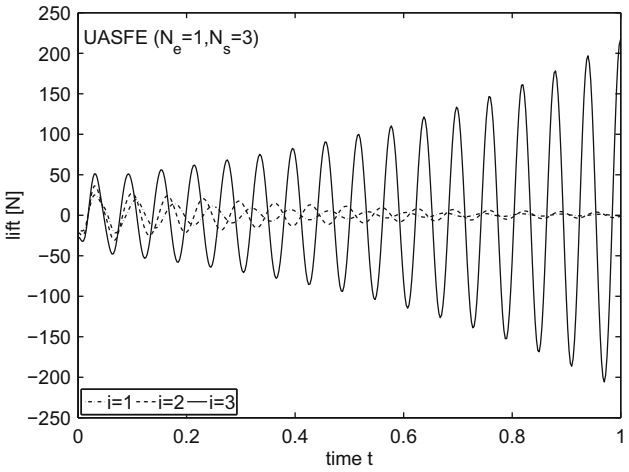

(a) lift samples $L_i(t)$

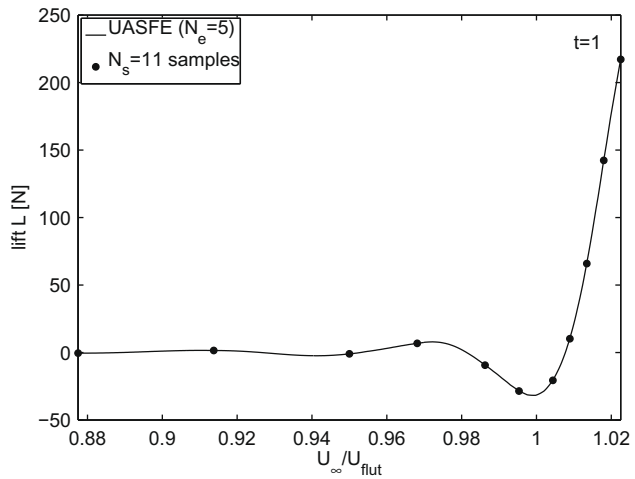

(b) lift response surface $L(t,\omega)$ at $t = 1$

Fig. 17. Results for the AGARD 445.6 wing with random free stream velocity $U_\infty(\omega)$.

safety factor. The coefficient of variation of the assumed unimodal beta distribution is set to $cv_{U_\infty} = 3.5\%$, see Fig. 16. The beta distribution is selected as a distribution on a finite domain with realistically zero probability at the endpoints of the interval. The outputs of interest are the lift $L(t,\omega)$ and the vertical tip displacement of the tip-node $y_{tip}(t,\omega)$.

The first $N_s = 3$ sampled time series of the lift $L_i(t,\omega)$ of the UASFE discretization with $N_e = 1$ element show in Fig. 17(a) that the first bending mode is the dominant mode in the system response. A second mode which is initially present in the response, damps out quickly, such that a wavelet decomposition pre-processing step is in this case not necessary to obtain the stochastic solution using UASFE. The samples illustrate that the free stream velocity has a significant effect on the frequency and the damping of the system response, which results in a diverging oscillation for $i = 3$, and decaying oscillations for $i = 1$ and mean value μ_{U_∞} at $i = 2$. The same conclusions can be drawn from Fig. 17(b) in which the response surface approximation of the lift $L(t,\omega)$ at $t = 1$ is given for $N_e = 5$ elements and $N_s = 11$ samples. Here the response surface is referred to as the output of interest L as function of the random input parameter U_∞/U_{flut}. The response surface has an oscillatory character due to the effect of the random $U_\infty(\omega)$ on the frequency of the lift oscillation and consequently on the phase differences in $L(t,\omega)$ at $t = 1$. The adaptive UASFE grid refinement results automatically in a gradually finer mesh in the region of large lift amplitudes at large values of $U_\infty(\omega)$.

Results for the time evolution of the mean $\mu_L(t)$ and the standard deviation $\sigma_L(t)$ of the lift are given in Fig. 18 for $N_e = 4$ and $N_e = 5$ elements. The two approximations are converged with respect to each other up to 5×10^{-3}. The time history for the mean lift $\mu_L(t)$ shows a decaying oscillation up to $t = 0.4$ s from the initial value of $\mu_L = -23.9$ N. This behavior can be explained by the decaying lift oscillation for a large range of $U_\infty(\omega)$ values and the effect of $U_\infty(\omega)$ on the increasing phase differences with time. For $t > 0.4$ the decay is approximately balanced by the exponentially increasing amplitude of the unstable part of the $U_\infty(\omega)$ parameter domain. In contrast, the standard deviation shows an oscillatory increase from the

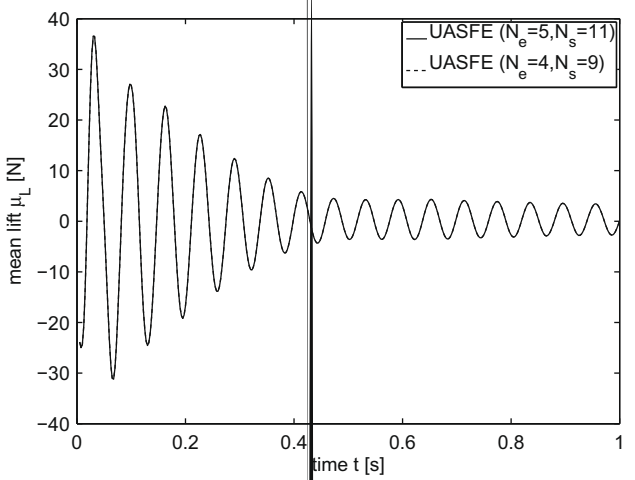

(a) mean μ_L

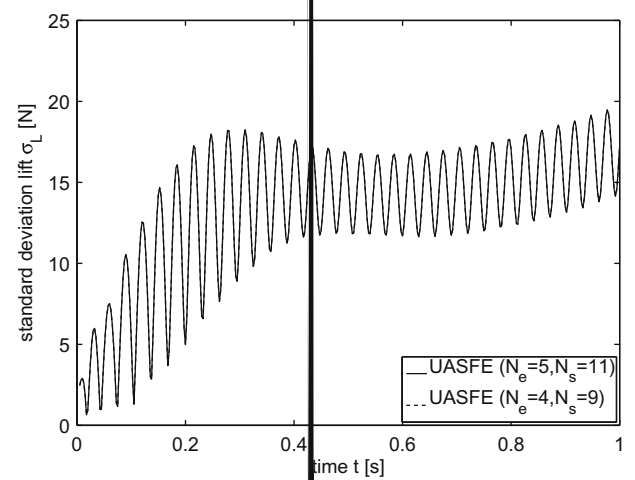

(b) standar

initial $\sigma_L = 2.46$ N up to a local maximum of $\sigma_L = 18.3$ N at $t = 0.31$ s due to the increasing phase differences with time. For $t > 0.31$ the standard deviation slightly decreases due to the decreasing lift amplitude in part of the parameter domain. Eventually, the unstable realizations result in an increasing standard deviation which reaches at $t = 1$ values between $\sigma_L = 14$ and $\sigma_L = 19$, which corresponds to an amplification of the initial standard deviation with a factor 6–8.

The nodal description of the structure directly returns the vertical tip-node displacement $y_{tip}(t,\omega)$. The approximations of the mean $\mu_{y_{tip}}(t)$ and standard deviation $\sigma_{y_{tip}}(t)$ of $y_{tip}(t,\omega)$ show in Fig. 19 a qualitatively similar behavior as the lift $L(t,\omega)$. The standard deviation $\sigma_{y_{tip}}(t)$ vanishes, however, initially due to the deterministic initial condition for the structure in contrast with the non-zero $\sigma_L(t)$ at $t = 0$. The standard deviation reaches values between $\sigma_{y_{tip}} = 4.2 \times 10^{-3}$ m and $\sigma_{y_{tip}} = 5.6 \times 10^{-3}$ m at $t = 1$, which corresponds to a standard deviation equal to 42% and 56% of the deterministic initial vertical tip deflection.

The probability of flutter can be determined by constructing the probability distribution of the damping factor of the system given in Fig. 20. The piecewise continuously differentiable function resulting from the piecewise polynomial approximation is more suited for representing the solution in terms of the cumulative distribution function and integral quantities like the probability of flutter. The probability density of Fig. 20(b) is derived from the cumulative distribution using a smoothing filter. The damping factor is here extracted from the last period of oscillation of the sampled vertical tip-node displacements. Positive and negative damping factors denote unstable and damped oscillatory responses, respectively. In other applications a positive damping factor is sometimes associated with stable motions. Even though the mean free stream velocity μ_{U_∞} is fixed at a safety margin of 5% below the deterministic flutter velocity U_{flut}, the non-zero probability of positive damping indicates a non-zero flutter probability. The 3.5% coefficient of variation of $U_\infty(\omega)$ results actually

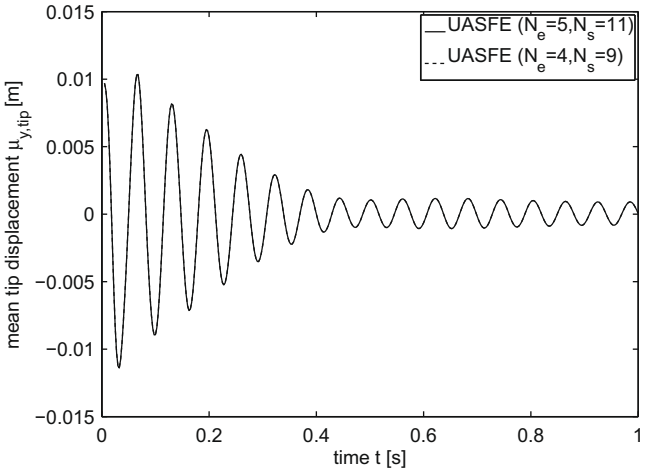

(a) mean $\mu_{y_{tip}}$

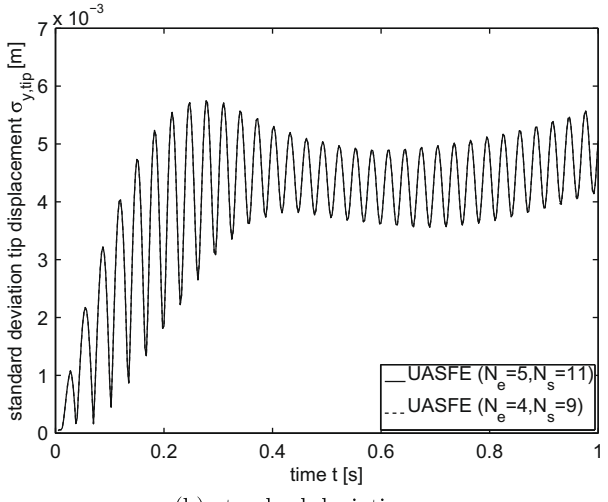

(b) standard deviation $\sigma_{y_{tip}}$

Fig. 19. Results for the AGARD 445.6 wing with random free stream velocity $U_\infty(\omega)$.

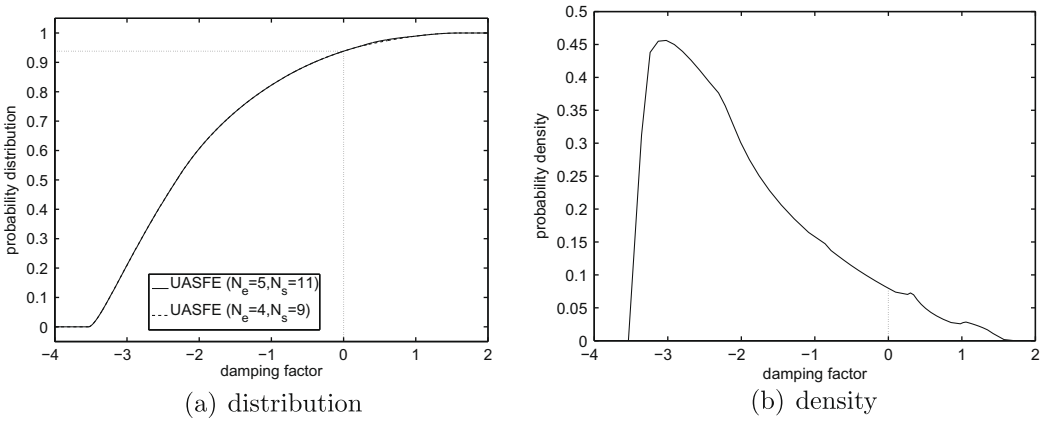

Fig. 20. Results for the AGARD 445.6 wing with random free stream velocity $U_\infty(\omega)$.

in a probability of flutter of 6.19%. Taking physical uncertainties into account in numerical predictions is often a more reliable approach than using safety margins in combination with deterministic simulation results.

4. Conclusions

The Unsteady Adaptive Stochastic Finite Elements (UASFE) method is extended to resolve the effect of randomness in aeroelastic simulations with multi-frequency responses and continuous structures by employing a wavelet decomposition pre-processing step. The sampled multi-frequency signals are decomposed into their single-frequency components in the wavelet analysis. The effect of the randomness on the single-mode components is determined by employing UASFE interpolation of the single-frequency signals at constant phase. This eliminates the effect of the increasing phase differences between the samples and consequently the increasing number of samples with time usually required by uncertainty quantification methods in time-dependent problems. The stochastic behavior of the multi-frequency response is, finally, obtained by summing the separate effects of the single-mode components. The actual interpolation is performed using a non-intrusive higher-order total variation diminishing Adaptive Stochastic Finite Elements (ASFE) approach based on Newton–Cotes quadrature in simplex elements. The resulting UASFE method is an efficient and robust approach for resolving the stochastic response of multi-frequency systems and continuous structures.

The application of UASFE to the multi-frequency response of a harmonically forced oscillator with randomness in the spring stiffness and the forcing frequency illustrates the effectiveness of the approach for this complex multi-scale stochastic problem by reducing the required number of samples by three orders of magnitude compared to Monte Carlo simulations. The UASFE discretization achieves a fourth-order error convergence with respect to the Monte Carlo reference solution for random spring stiffness. The study of a multi-mode response of a continuous plate structure in supersonic flow with a random plate density and a random field modulus of elasticity shows a qualitatively different stochastic behavior of the potential and kinetic energy of the plate for the two sources of randomness. The diverging mean and standard deviation of the total structural energy are two orders of magnitude more sensitive to variations in the modulus of elasticity than the plate density, which results in an amplification of the input coefficient of variation by a factor 485 at $t = 0.4$. The results for the aeroelastic simulation of the three-dimensional transonic AGARD 445.6 wing with random free stream velocity illustrate that, although the mean free stream velocity is a safety margin of 5% below the deterministic flutter velocity, a 3.5% coefficient of variation still results in a non-zero flutter probability of 6.19%.

Acknowledgments

This research was supported by the Technology Foundation STW, applied science division of NWO and the technology programme of the Ministry of Economic Affairs.

References

[1] I.M. Babuška, R. Tempone, G.E. Zouraris, Galerkin finite element approximations of stochastic elliptic partial differential equations, SIAM J. Numer. Anal. 42 (2) (2004) 800–825.
[2] I.M. Babuška, F. Nobile, R. Tempone, A stochastic collocation method for elliptic partial differential equations with random input data, SIAM J. Numer. Anal. 45 (3) (2007) 1005–1034.
[3] R. Beaubien, F. Nitzsche, D. Feszty, Time and frequency domain solutions for the AGARD 445 wing, in: Proceedings of the International Forum on Aeroelasticity and Structural Dynamics (IFASD), Munich, Germany, 2005.
[4] P.S. Beran, C.L. Pettit, D.R. Millman, Uncertainty quantification of limit cycle oscillations, J. Comput. Phys. 217 (1) (2006) 217–247.
[5] A. de Boer, M.S. van der Schoot, H. Bijl, Mesh deformation based on radial basis function interpolation, Comput. Struct. 85 (2007) 784–795.

[6] F. Casciati, B. Roberts, Mathematical Models for Structural Reliability Analysis, CRC Press, Boca Raton, 1996.
[7] A.J. Chorin, J.E. Marsden, A Mathematical Introduction to Fluid Mechanics, Springer-Verlag, New York, 1979.
[8] L. Cohen, Time–Frequency Analysis, Prentice-Hall, 1995.
[9] R. Coifman, M.V. Wickerhauser, Wavelets and adapted waveform analysis, in: Proceedings of the Symposia in Applied Mathematics, vol. 47, American Mathematical Society, Providence, RI, 1991, pp. 119–154.
[10] I. Daubechies, Ten Lectures on Wavelets, Society for Industrial and Applied Mathematics, Philadelphia, 1992.
[11] M.K. Deb, I.M. Babuška, J.T. Oden, Solution of stochastic partial differential equations using Galerkin finite element techniques, Comput. Method Appl. Mech. Eng. 190 (2001) 6359–6372.
[12] E.H. Dowell, Aeroelasticity of Plates and Shells, Noordhoff International Publishing, Leyden, 1975.
[13] R.G. Ghanem, P.D. Spanos, Stochastic Finite Elements: A Spectral Approach, Springer-Verlag, New York, 1991.
[14] J.M. Hammersley, D.C. Handscomb, Monte Carlo methods, Methuen's Monographs on Applied Probability and Statistics, Methuen, London, 1964.
[15] A. Harten, High resolution schemes for hyperbolic conservation laws, J. Comput. Phys. 49 (1983) 357–393.
[16] S. Hosder, R.W. Walters, R. Perez, A non-intrusive polynomial chaos method for uncertainty propagation in CFD simulations, in: Proceedings of the 44th AIAA Aerospace Sciences Meeting and Exhibit, AIAA-2006-891, Reno, NV, 2006.
[17] C. Kennedy, M. Carpenter, Additive Runge–Kutta schemes for convection–diffusion–reaction equations, Appl. Numer. Math. 44 (2003) 139–181.
[18] B. Koobus, C. Farhat, Second-order time-accurate and geometrically conservative implicit schemes for flow computations on unstructured dynamic meshes, Comput. Method Appl. Mech. Eng. 170 (1999) 103–129.
[19] O.P. Le Maître, O.M. Knio, H.N. Najm, R.G. Ghanem, Uncertainty propagation using Wiener–Haar expansions, J. Comput. Phys. 197 (2004) 28–57.
[20] O.P. Le Maître, H.N. Najm, R.G. Ghanem, O.M. Knio, Multi-resolution analysis of Wiener-type uncertainty propagation schemes, J. Comput. Phys. 197 (2004) 502–531.
[21] M. Loève, Probability Theory, fourth ed., Springer-Verlag, New York, 1977.
[22] H. Madsen, S. Krenk, N.C. Lind, Methods of Structural Safety, Prentice-Hall, Englewood Cliffs, 1986.
[23] L. Mathelin, M.Y. Hussaini, Th.A. Zang, Stochastic approaches to uncertainty quantification in CFD simulations, Numer. Algor. 38 (1–3) (2005) 209–236.
[24] D.R. Millman, P.I. King, P.S. Beran, Airfoil pitch-and-plunge bifurcation behavior with Fourier chaos expansions, J. Aircraft 42 (2005) 376–384.
[25] Openfem – A finite element toolbox for Matlab and Scilab, 2006. <http://www.rocq.inria.fr/OpenFEM/>.
[26] C.L. Pettit, P.S. Beran, Spectral and multiresolution Wiener expansions of oscillatory stochastic processes, J. Sound Vib. 294 (2006) 752–779.
[27] M.T. Reagan, H.N. Najm, R.G. Ghanem, O.M. Knio, Uncertainty quantification in reacting-flow simulations through non-intrusive spectral projection, Combust. Flame 132 (2003) 545–555.
[28] M.A. Tatang, Direct incorporation of uncertainty in chemical and environmental engineering systems, Ph.D. Thesis, MIT, Cambridge, 1995.
[29] C.V. Verhoosel, M.A. Gutirrez, S.J. Hulshoff, Iterative solution of the random eigenvalue problem with application to spectral stochastic finite element systems, Int. J. Numer. Method Eng. 68 (4) (2006) 401–424.
[30] G.G. Walter, Wavelets and Other Orthogonal Systems with Applications, Chapman and Hall/CRC, Boca Raton, 2001.
[31] X.L. Wan, G.E. Karniadakis, An adaptive multi-element generalized polynomial chaos method for stochastic differential equations, J. Comput. Phys. 209 (2) (2005) 617–642.
[32] J.A.S. Witteveen, H. Bijl, A monomial chaos approach for efficient uncertainty quantification in nonlinear problems, SIAM J. Sci. Comput. 30 (2008) 1296–1317.
[33] J.A.S. Witteveen, G.J.A. Loeven, S. Sarkar, H. Bijl, Probabilistic collocation for period-1 limit cycle oscillations, J. Sound Vib. 311 (1-2) (2008) 421–439.
[34] J.A.S. Witteveen, H. Bijl, Efficient quantification of the effect of uncertainties in advection–diffusion problems using polynomial chaos, Numer. Heat Tr. B: Fund. 53 (2008) 437–465.
[35] J.A.S. Witteveen, H. Bijl, An unsteady adaptive stochastic finite elements formulation for rigid-body fluid–structure interaction, Comput. Struct. 86 (2008) 2123–2140.
[36] J.A.S. Witteveen, H. Bijl, An alternative unsteady adaptive stochastic finite elements formulation based on interpolation at constant phase, Comput. Method Appl. Mech. Eng. 198 (2008) 578–591.
[37] J.A.S. Witteveen, G.J.A. Loeven, H. Bijl, An adaptive stochastic finite elements approach based on Newton–Cotes quadrature in simplex elements, Comput. Fluid 38 (2009) 1270–1288.
[38] J.A.S. Witteveen, H. Bijl, A TVD uncertainty quantification method with bounded error applied to transonic airfoil flutter, Commun. Comput. Phys. 6 (2009) 406–432.
[39] D.B. Xiu, G.E. Karniadakis, The Wiener–Askey polynomial chaos for stochastic differential equations, SIAM J. Sci. Comput. 24 (2) (2002) 619–644.
[40] E. Yates Jr., AGARD standard aeroelastic configurations for dynamic response, Candidate configuration I-Wing 445.6, Technical Memorandum 100492, NASA, 1987.
[41] A.H. van Zuijlen, H. Bijl, Implicit and explicit higher-order time integration schemes for structural dynamics and fluid–structure interaction computations, Comput. Struct. 83 (2-3) (2005) 93–105.
[42] A.H. van Zuijlen, H. Bijl, Implicit and explicit higher-order time integration schemes for fluid–structure interaction computations, Int. J. Multiscale Comput. Eng. 4 (2) (2006) 255–263.
[43] A.H. van Zuijlen, A. de Boer, H. Bijl, Higher-order time integration through smooth mesh deformation for 3D fluid–structure interaction simulations, J. Comput. Phys. 224 (2007) 414–430.